PHYSICAL REVIEW A **93**, 033825 (2016)

Attosecond lighthouses in gases: A theoretical and numerical study

T. Auguste,[*] O. Gobert, T. Ruchon, and F. Quéré

Lasers, Interactions and Dynamics Laboratory (LIDyL), CEA, CNRS, Université Paris-Saclay, CEA Saclay, 91191 Gif sur Yvette, France

(Received 10 December 2015; published 10 March 2016)

We present an extensive theoretical and numerical study of the attosecond lighthouse effect in gases. We study how this scheme impacts the spatiotemporal structure of the driving laser field all along the generation medium, and show that this can modify the phase matching relation governing high-harmonic generation (HHG) in gases. We then present a set of numerical simulations performed to test the robustness of the effect against variations of HHG parameters, and to identify possible solutions for relaxing the constraint on the driving laser pulse duration. We thus demonstrate that the lighthouse effect can actually be achieved with laser pulses consisting of up to ∼8 optical periods available from current lasers without postcompression, for instance by using an appropriate combination of 800- and 1600-nm wavelength fields.

DOI: 10.1103/PhysRevA.93.033825

I. INTRODUCTION

In the past decade, attosecond metrology has enabled the development ([1] and references therein) and characterization [2,3] of attosecond light sources, for probing electron dynamics in atoms [4], molecules [5], and solids [6] with an unprecedented time resolution. Attosecond pulse trains are naturally released during HHG with multicycle lasers. However, so far, most of the applications used pump-probe schemes that require single attosecond pulses. Such isolated bursts remain difficult to produce routinely, because they necessitate to use either extremely short phase-stabilized driving laser pulses (∼4 fs), with [7,8], or without [9] a polarization gate, or multicycle laser pulses (∼30 fs) using a two-color gating scheme [10–12] or by combining a polarization gate with two-color mixing [13,14].

An approach called the attosecond lighthouse scheme, that uses space-time couplings (STCs) on the driving laser, has recently been demonstrated. STCs [15], which are often considered spurious effects in laser physics, are used here to angularly separate the successive pulses of the attosecond pulse train produced with a multicycle laser pulse. Proposed [16] and observed [17] for HHG on plasma mirrors, it was rapidly generalized to HHG in gases [18,19]. Very recently, the method was also demonstrated with driving lasers in the midinfrared wavelength range [20,21], thus enabling the production of single attosecond pulses with spectra extending up to the water window [21]. Note that besides the generation of isolated attosecond pulses, a major interest of this effect is the spatial encoding of the attosecond pulse train, which makes it possible to use the HH signal to probe electron dynamics, e.g., in molecules, on a single pump laser shot with a time resolution of half a laser period—a measurement scheme called photonic streaking [18,19].

This paper presents an extensive theoretical and numerical study of the attosecond lighthouse effect in gases, and is organized as follows: In Sec. II, we first briefly remind of the general principle of the attosecond lighthouse effect, which exploits laser beams with a STC at focus known as wave-front rotation (WFR), induced by applying pulse front tilt (PFT) to the beam prior to focusing. Because this effect was discovered in the context of HHG from plasma mirrors, where generation occurs in the focal plane, its initial analysis only considered the space-time structure of the laser field exactly at focus. The situation is very different for HHG in gases, where the generation occurs over a certain propagation distance around focus. A proper understanding of the attosecond lighthouse scheme in gases thus requires an analysis of the modifications induced by STC on the amplitude and phase of the driving laser along its propagation direction. We provide such an analysis in Sec. III using analytical expressions, and qualitatively discuss the consequences on HHG in gases, in particular on its phase-matching conditions. The second half of the paper is dedicated to numerical simulations. In Sec. IV, we briefly describe the numerical model used for simulating HHG in gases, and present a simulation of the lighthouse effect that will be used as a reference case in the rest of the paper. Section V presents the results of a parametric study performed using this numerical model. Section V A is devoted to the study of the influence of HHG parameters on the lighthouse effect. We show that the phase-matching relation, which rules HHG in gases, is modified due to STC introduced on the laser pulse. Section V B proposes and demonstrates solutions to relax the constraints on the driving laser pulse duration required to obtain attosecond lighthouses in gases. A summary of the results is provided in Sec. VI.

II. PRINCIPLE OF THE ATTOSECOND LIGHTHOUSE EFFECT

The attosecond lighthouse effect relies on the use of a laser field whose propagation direction rotates in time at focus, on the femtosecond scale. This space-time coupling corresponds to a temporal rotation of the field wave-front. In these conditions, attosecond pulses produced in successive cycles (or half cycles in the case of gases) of the laser pulse propagate in slightly different directions, and can be angularly separated in the far field if the wave-front rotation velocity is large enough.

Such a temporal wave-front rotation at focus can be induced by using a laser beam described by the following electric field

[*]Corresponding author: thierry.auguste@cea.fr

prior to focusing:

$$E_i(x_i,y_i,t) = E_i^0 \exp\left[-\frac{\alpha^2(t+\xi x_i)^2}{\tau_L^2}\right] \times \exp\left[-\frac{x_i^2+y_i^2}{R^2}\right]\exp[i(\omega_L t+\phi_0)], \quad (1)$$

where E_i^0 is the peak electric field and $\alpha = \sqrt{2\times\ln(2)}$. R is the beam waist. x_i and y_i are the transverse coordinates in the plane of incidence and t is the time coordinate. τ_L is the full width at half maximum (FWHM) Fourier-transform limited pulse duration, ω_L is the pulse central frequency, and ϕ_0 is the carrier-envelope phase (CEP). ξ is a STC parameter known as pulse front tilt (PFT), expressed in [s/m]. It accounts for a tilt between the beam wave front and pulse front.

We consider throughout the paper a linearly polarized laser, propagating along the z axis, in the positive z direction. We assume that the field is Gaussian in time, as well as in space, unless otherwise stated. Moreover, since STC only operates on the x_i spatial transverse coordinate, we restrict our analysis to this coordinate, thus dramatically reducing the computation time in the simulations presented in Sec. V. We therefore disregard the y dependence in all the equations of Secs. III and IV.

Once focused, such a laser field does not present any more PFT in the focal plane, but only wave-front rotation (WFR). To demonstrate this, we now calculate the electric field at the focus of an optics of focal length f, which is the spatial Fourier transform of the incident field $E_i(x_i,t)$. By doing so, we implicitly assume that the optical element or system used for producing PFT, for example a glass wedge, is placed in the object focal plane of the focusing optics [22]. When this is not the case, the different frequencies composing the laser pulse can start separating spatially (spatial chirp) before reaching this object focal plane, and this additional STC then has to be taken into account in the calculation of the field. This additional effect, which can modify the position of the plane where pure WFR is obtained, will be discussed in a forthcoming article. In our case, the field $E_f(x_f,t)$ in the focal plane writes

$$E_f(x_f,t) = E_f^0 \exp\left\{-\frac{x_f^2}{w_0^2[1+(\alpha\xi R/\tau_L)^2]}\right\} \times \exp\left\{-\frac{\alpha^2 t^2}{\tau_L^2[1+(\alpha\xi R/\tau_L)^2]}\right\} \times \exp[i\phi_f(x_f,t)], \quad (2)$$

with

$$\phi_f(x_f,t) = \omega_L t + \zeta_f x_f t + \phi_0, \quad (3)$$

with $\zeta_f = \frac{2\alpha^2\xi R}{w_0\tau_L^2[1+(\alpha\xi R/\tau_L)^2]}$. $w_0 = \frac{\lambda_L f}{\pi R}$ is the usual diffraction limited beam waist at focus. λ_L and x_f denote respectively the laser wavelength and the transverse coordinate in the focal plane. $E_f^0 = \sqrt{\frac{R}{iw_0}}\frac{E_i^0\exp(i\frac{2\pi f}{\lambda_L})}{\sqrt{1+(\alpha\xi R/\tau_L)^2}}$ is the peak electric field at focus. The instantaneous direction of propagation of light, β, is given by $\beta \simeq \frac{k_\perp}{k_L}$ [16], where $k_L = \frac{2\pi}{\lambda_L}$ is the laser wave vector and $k_\perp = \frac{\partial\phi_f}{\partial x_f}$ is its transverse component. For the field of Eq. (2), β, and therefore the instantaneous wave-front direction, depends on time. This is the key effect used in the attosecond lighthouse scheme. The WFR velocity, v_r[rad/s], is given by

$$v_r(\xi) = \frac{d\beta}{dt} = \frac{\zeta_f}{k_L} = \frac{\alpha^2 R^2}{f\tau_L^2}\frac{\xi}{1+(\alpha\xi R/\tau_L)^2}. \quad (4)$$

The effective waist, w_{eff}, and pulse duration, τ_{eff}, of the beam at focus are given by

$$w_{\text{eff}} = w_0\sqrt{1+(\alpha\xi R/\tau_L)^2}, \quad (5)$$

and

$$\tau_{\text{eff}} = \frac{\tau_L}{\alpha}\sqrt{1+(\alpha\xi R/\tau_L)^2}. \quad (6)$$

Due to the PFT ξ initially applied on the laser beam, both parameters are increased compared to the nominal case where $\xi = 0$. As a result, the peak intensity at focus, $I_f^0 = \frac{1}{2}\epsilon_0 c|E_f^0|^2$, is also reduced, by a factor $1+(\alpha\xi R/\tau_L)^2$. From an experimental point of view, this is the price to pay to obtain WFR at focus.

An essential feature of the WFR velocity given by Eq. (4) is that it reaches a maximum of $v_r^{\max} = \frac{\alpha R}{2f\tau_L}$, for $\xi_{\max} = \frac{\tau_L}{\alpha R}$. When $v_r = v_r^{\max}$, the laser intensity at focus is only half the one reached with $\xi = 0$. We have plotted in Fig. 1 the WFR velocity at focus as a function of the STC parameter ξ for three values of the laser pulse duration τ_L. Calculations are performed for a 1-m focal length optics and a 25-mm incident beam waist. The rotation velocity is maximum for $\tau_L = 5$ fs (black squares). The corresponding optimum coupling parameter is $\xi_{\max} = 0.17$ fs/mm. As expected from the expression of $v_r^{\max}$, doubling the pulse duration leads to an optimum coupling parameter twice the one obtained with 5-fs duration pulse (empty circles), and the maximum WFR velocity is divided by 2. On the other hand, the curve flattens with increasing pulse duration. For 20-fs pulse duration (black stars), v_r is almost constant for ξ greater than 0.4 fs/mm. In the following, the calculations are performed with the maximum WFR velocity obtained for $\xi_{\max}$, unless otherwise stated.

Attosecond lighthouses consist of N well-separated beamlets in the far field, each of them carrying a single attosecond pulse. For separating adjacent beamlets, the rotation $\Delta\beta = v_r\Delta t$ of the wave-front in the time interval Δt between the emission of two successive attosecond pulses must be larger than the divergence θ_q of light beam around frequency $q\omega$. In the optimal case, i.e., when $v_r = v_r^{\max}$, this leads to the following condition:

$$\frac{\theta_q}{\theta_L} \lesssim \frac{1}{pN_{\text{cycle}}}, \quad (7)$$

where $\theta_L = \frac{R}{f}$ is the laser beam divergence, and $N_{\text{cycle}} = \frac{\tau_L}{\alpha T_L}$ is the number of optical cycles in the pulse. T_L is the laser period and p is the number of attosecond pulses emitted per cycle ($p = 2$ for gases and $p = 1$ for plasma mirrors). Therefore, assuming the same ratio of harmonic and laser divergence, attosecond lighthouses in gases necessitate laser pulses twice shorter than those required for plasma mirrors. Note that the divergence θ_q involved in condition (7) is actually the one obtained in the presence of WFR, which can be different from

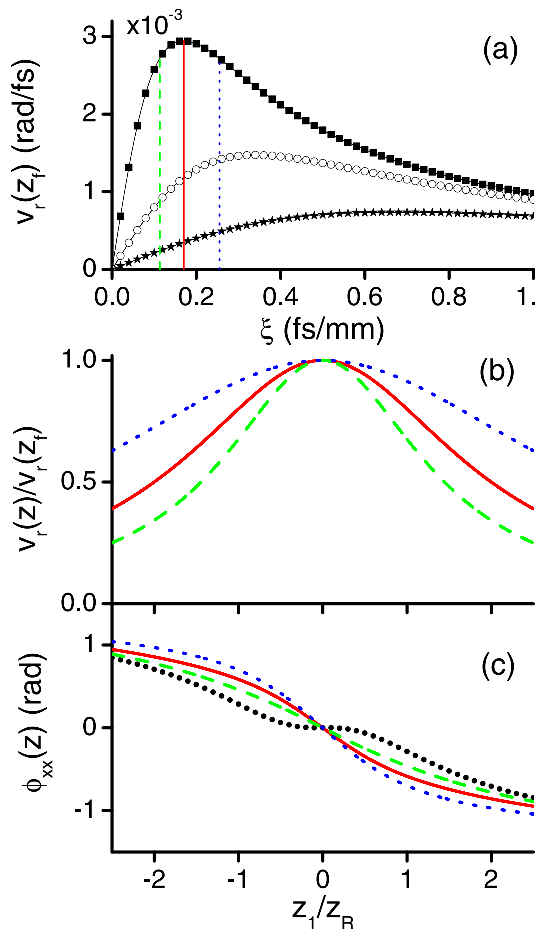

FIG. 1. (a) WFR velocity as a function of STC parameter ξ calculated for $\tau_L = 5$ fs (black squares), 10 fs (empty circles), and 20 fs (black stars). (b) Normalized WFR velocity as a function of the distance to the focus $z_1 = z - z_f$ (in units of z_R), for $\tau_L =$ 5-fs and for $\xi = 2/3 \times \xi_{\max}$ (dashed green line), $\xi_{\max}$ (solid red line) and $3/2 \times \xi_{\max}$ (dotted blue line). The corresponding WFR velocities in $z_1 = 0$ are indicated by the vertical lines in (a). (c) Variation of the phase with the distance to the focus in $x = w_0$, with the same parameters and same color codes and symbols as in (b). The curve with black circles depicts the phase of a focused regular Gaussian beam.

the one obtained with a standard STC-free driving laser beam (see Fig. 3 in Sec. III).

III. ANALYTICAL DESCRIPTION OF THE LASER FIELD

When a laser beam with PFT is focused, there is a gradual transition from this initial PFT to WFR at focus, over a distance of the order of the Rayleigh length. In the case of harmonic generation in gases, the condition given by Eq. (7), although necessary, may thus not be sufficient to ensure a good separation of adjacent beamlets in the far field, because the harmonic field builds up while copropagating with the driving field, over distances such that the spatiotemporal structure of the laser field can evolve. It is therefore necessary to consider this spatiotemporal structure out of focus. We calculate the field at a distance $z_1 = z - z_f$ from the focus by means of the Huygens-Fresnel integral. It is convenient to perform the calculation in the frequency domain. To start, we thus calculate the time Fourier transform of the field at focus [Eq. (2)]:

$$E_f(x_f,\omega) = \frac{\tau_{\text{eff}}\sqrt{\pi}}{\alpha} E_f^0 \exp\left[-\frac{x_f^2}{w_{\text{eff}}^2}\right] \times \exp\left[-\frac{\tau_{\text{eff}}^2}{4\alpha^2}(\zeta_f x_f + \omega - \omega_L)^2\right]. \tag{8}$$

The field at each point of coordinates (x, z) is then given by

$$E(x,\omega,z) \propto \exp\left[-\frac{x^2}{w(z)^2}\right] \exp\left[-\frac{\tau(z)^2}{4}[\zeta(z)x + \omega - \omega_L]^2\right] \times \exp\left[i\frac{\phi^{(2)}(z)}{2}(\omega - \omega_L)^2 + i\psi(z)x(\omega - \omega_L)\right]. \tag{9}$$

Note that $E(x,\omega,z_f) \equiv E_f(x_f,\omega)$. $w(z)$ is the laser beam waist at position z along the propagation axis, given by

$$w(z) = w_0\sqrt{1 + \left(\frac{\alpha\xi R}{\tau_L}\right)^2 + \left(\frac{z_1}{z_R}\right)^2} \tag{10}$$

$$= w_{\text{eff}}\sqrt{1 + \left(\frac{z_1}{z_R w_{\text{eff}}/w_0}\right)^2} \tag{11}$$

with $z_R = \frac{\pi w_0^2}{\lambda_L}$ the Rayleigh range corresponding to $\xi = 0$. Similarly to the effective waist [Eq. (5)], one can thus define an effective Rayleigh range, a key parameter for HHG in gases:

$$z_R^{\text{eff}} = \frac{\pi w_0 w_{\text{eff}}}{\lambda_L} = z_R\sqrt{1 + \left(\frac{\alpha\xi R}{\tau_L}\right)^2}. \tag{12}$$

Note that the beam waist and associated Rayleigh range are unaffected for the other transverse spatial coordinate y_f. $\tau(z)$ is the local Fourier-transform limited pulse duration:

$$\tau(z) = \frac{\tau_L}{\alpha}\sqrt{\frac{1 + \left(\frac{\alpha\xi R}{\tau_L}\right)^2 + \left(\frac{z_1}{z_R}\right)^2}{1 + \left(\frac{z_1}{z_R}\right)^2}}. \tag{13}$$

For $z = z_f$ ($z_1 = 0$) in Eqs. (10) and (13), we recover Eqs. (5) and (6). The spatial chirp $\zeta(z)$ at position z is given by

$$\zeta(z) = \zeta_f \frac{1 + \left(\frac{\alpha\xi R}{\tau_L}\right)^2}{1 + \left(\frac{\alpha\xi R}{\tau_L}\right)^2 + \left(\frac{z_1}{z_R}\right)^2}. \tag{14}$$

By taking $z = z_f$, one recovers $\zeta(z_f) = \zeta_f$. The z-dependent PFT parameter $\psi(z)$ writes

$$\psi(z) = \frac{(f/z_R^2)\xi z_1}{1 + \left(\frac{z_1}{z_R}\right)^2}. \tag{15}$$

This equation shows that there is no PFT at focus [$\psi(z_f) = 0$], as previously mentioned. The $\phi^{(2)}(z)$ term, corresponding to the frequency chirp induced by the propagation of the laser spectral components in different directions, is written

$$\phi^{(2)}(z) = \frac{(f/z_R)^2\xi^2 z_1}{k_L\left[1+\left(\frac{z_1}{z_R}\right)^2\right]}. \quad (16)$$

One can note that there is no frequency chirp at focus ($z_1 = 0$) and far from it ($z \longrightarrow \infty$).

Coming back to the time domain by calculating the Fourier transform of Eq. (9) with respect to ω, we split the spatiotemporal phase into three parts:

$$\Phi(x,t,z) = \phi_{xt}(z) - \phi_{xx}(z) + \phi_{tt}(z). \quad (17)$$

Using Eqs. (13)–(16), we derive $\phi_{xt}(z) = v_r(z)t$, with $v_r(z)$ the z-dependent WFR velocity given by

$$v_r(z) = \frac{1}{k_L}\frac{\tau(z)^4\zeta(z) + 8\psi(z)\phi^{(2)}(z)}{\tau(z)^4 + 16[\phi^{(2)}(z)]^2}. \quad (18)$$

By rewriting $v_r(z)$ as a function of $(\frac{\alpha\xi R}{\tau_L})^2$ and $\frac{z_1}{z_R}$, it gives

$$v_r(z) = \frac{\zeta_f}{k_L}\frac{\left[1+\left(\frac{\alpha\xi R}{\tau_L}\right)^2\right]^2\left[1+\left(\frac{z_1}{z_R}\right)^2\right]}{\left[1+\left(\frac{\alpha\xi R}{\tau_L}\right)^2+\left(\frac{z_1}{z_R}\right)^2\right]^2+\left(\frac{\alpha\xi R}{\tau_L}\right)^4\left(\frac{z_1}{z_R}\right)^2}. \quad (19)$$

As expected, for $z = z_f$, $v_r = \frac{\zeta_f}{k_L}$. Letting $z \longrightarrow \infty$ leads to $v_r \longrightarrow 0$, confirming that there is no WFR far from the focus. Figure 1(b) displays the relative WFR velocity as a function of the distance from the focus normalized to the Rayleigh range. The calculation is performed for a 5-fs initial pulse duration, for three values of the coupling ξ parameter, equal to $2/3 \times \xi_{\max}$, $\xi_{\max}$, and $3/2 \times \xi_{\max}$, depicted respectively by green, red and blue lines. The two parameters $\xi = 2/3 \times \xi_{\max}$ and $3/2 \times \xi_{\max}$ lead to the same WFR velocity right at focus, that corresponds to 90% of $v_r^{\max}$, as shown by the vertical dashed lines in Fig. 1(a). However, the variation of v_r with the distance to the focus z_1 is very different in the two cases, becoming stronger as ξ decreases. In $z = \pm z_R$, the WFR velocity drops to $0.7 \times v_r(z_f)$ ($0.6 \times v_r^{\max}$) for $\xi = 2/3 \times \xi_{\max}$ while it is still $0.9 \times v_r(z_f)$ ($0.8 \times v_r^{\max}$) for $\xi = 3/2 \times \xi_{\max}$. This is due to the increase of the beam waist [see Eq. (5)], and consequently the Rayleigh range, with ξ. Hence, one must emphasize that two different values of ξ giving the same WFR velocity at focus do not lead to the same evolution of the laser pulse out of focus—larger ξ leading to a slower evolution that should be more favorable for HHG in gases.

The application of PFT on the unfocused beam also gives rise to an additional term in the laser spatial phase $\phi_{xx}(z)$ which then writes as

$$\phi_{xx}(z) = \frac{x^2}{w_0^2}\frac{z_1/z_R}{1+(z_1/z_R)^2} - \tan^{-1} z_1/z_R + x^2\frac{\tau(z)^4\zeta(z)[\zeta(z)\phi^{(2)}(z) - \psi(z)] - 4\psi(z)^2\phi^{(2)}(z)}{\tau(z)^4 + 16[\phi^{(2)}(z)]^2}, \quad (20)$$

where the two first terms on the right-hand side of the equality are the usual phase terms for a focused regular Gaussian beam; the first corresponds to wave-front curvature, and the second one, independent of the transverse coordinate x, is the well-known Gouy phase. The third term is exclusively due to the presence of STC. After replacing $\tau(z)$, $\psi(z)$, $\zeta(z)$, and $\phi^{(2)}(z)$ in Eq. (20) by their expression as a function of $(\frac{\alpha\xi R}{\tau_L})^2$ and $\frac{z_1}{z_R}$, and after some simplifications, we finally get

$$\phi_{xx}(z) = \frac{x^2}{w_0^2}\frac{z_1}{z_R}\frac{1+\left\{2+\left(\frac{\alpha\xi R}{\tau_L}\right)^2\left[1-\left(\frac{\alpha\xi R}{\tau_L}\right)^2\right]\right\}\left(\frac{z_1}{z_R}\right)^2+\left(\frac{z_1}{z_R}\right)^4}{\left[1+\left(\frac{z_1}{z_R}\right)^2\right]\left\{\left[1+\left(\frac{\alpha\xi R}{\tau_L}\right)^2+\left(\frac{z_1}{z_R}\right)^2\right]^2+\left(\frac{\alpha\xi R}{\tau_L}\right)^4\left(\frac{z_1}{z_R}\right)^2\right\}} - \tan^{-1} z_1/z_R. \quad (21)$$

The off–axis phase is significantly modified by STC, as shown in Fig. 1(c), which displays $\phi_{xx}(z)$ for $x = w_0$. Calculations are performed for the same values of coupling parameter and are displayed with the same color codes and symbols as in Fig. 1(b). For $-0.5 \leqslant z_1/z_R \leqslant +0.5$, this phase varies linearly with z, with a slope larger in magnitude than in the absence of STC (black circles) that increases with ξ.

Finally, the last term on the right-hand side of equality (17) is the z-dependent temporal chirp, given by

$$\phi_{tt}(z) = \frac{4\phi^{(2)}(z)t^2}{\tau(z)^4 + 16[\phi^{(2)}(z)]^2}. \quad (22)$$

When replacing $\phi^{(2)}(z)$ by expression (16), we obtain

$$\phi_{tt}(z) = \frac{\alpha^2 t^2}{\tau_L^2}\frac{z_1}{z_R}\frac{\left(\frac{\alpha\xi R}{\tau_L}\right)^2\left[1+\left(\frac{z_1}{z_R}\right)^2\right]}{\left[1+\left(\frac{\alpha\xi R}{\tau_L}\right)^2+\left(\frac{z_1}{z_R}\right)^2\right]^2+\left(\frac{\alpha\xi R}{\tau_L}\right)^4\left(\frac{z_1}{z_R}\right)^2}. \quad (23)$$

To illustrate the effect of STC on the laser pulse while propagating, we have reported in Fig. 2 the space-time distribution of the electric field, $E(x,t,z)$, calculated at four positions z along the propagation axis. We consider an incident laser beam of 25-mm waist and 5-fs FWHM Fourier-transform limited pulse duration, focused by a $f = 1$ m optics. The waist at focus is $w_0 = 10\ \mu$m, and the Rayleigh range is $z_R = 400\ \mu$m. The STC parameter is 0.17 fs/mm. Figure 2(a) displays the laser field distribution at focus. One clearly sees wave-front rotation in time. As the laser beam propagates, PFT appears and progressively dominates on WFR, as can be observed in Figs. 2(b)–2(d), computed for propagation distances of respectively $0.5 \times z_R$, $1.0 \times z_R$, and $2.5 \times z_R$.

From the results summarized in Figs. 1 and 2, one can anticipate that the evolution of the spatiotemporal shape of the field out of the best focus will complicate the attosecond lighthouse effect in gases, compared to the case of plasma mirrors. This will most likely be detrimental when the length of the generation medium or its distance to the best focus become comparable or larger than the effective Rayleigh length z_R^{eff}. On the other hand, the increase in effective Rayleigh length resulting of the application of PFT can be beneficial for the HHG efficiency. To study these different effects quantitatively, we now turn to a numerical model of HHG in gases, described in the next section.

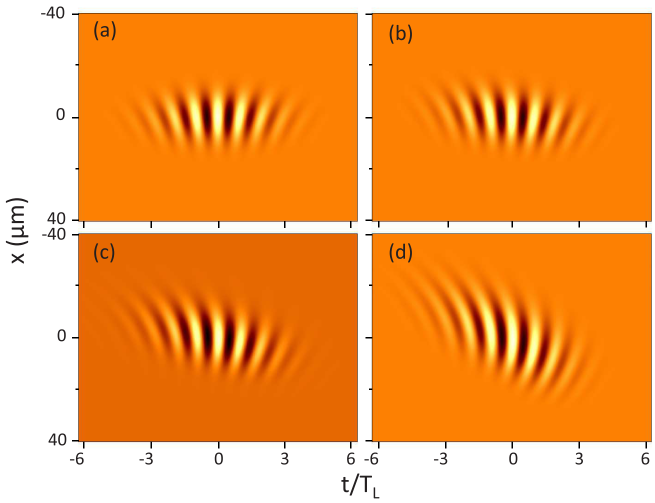

FIG. 2. Space-time laser electric-field distribution calculated for $\tau_L = 5$ fs, $\xi = 0.17$ fs/mm, and $z_R = 400\ \mu$m. (a) Distributions at focus and (b) after propagation on distances of $0.5 \times z_R$, (c) $1.0 \times z_R$, and (d) $2.5 \times z_R$. Time is normalized to the laser period T_L.

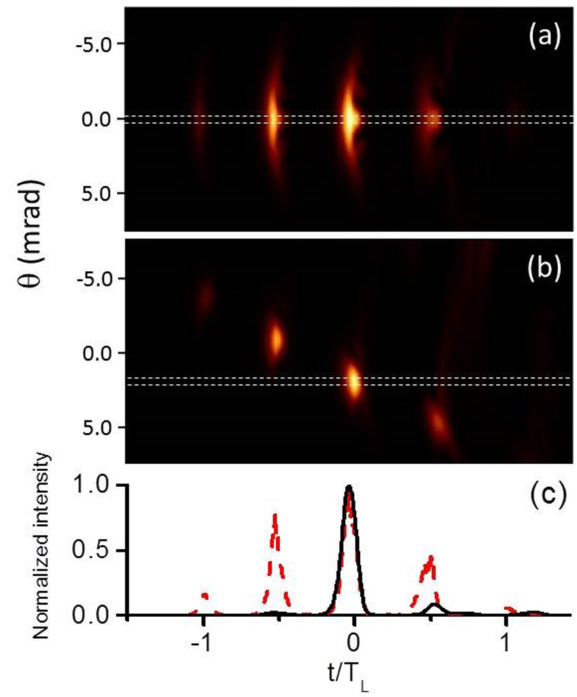

FIG. 3. Far-field space-time square modulus of the attosecond pulse electric fields generated by a laser beam (a) without WFR ($\xi = 0$) and (b) using pulse parameters of Fig. 2. In both (a) and (b), the peak intensity in the middle of the jet is 8.65×10^{14} W/cm^2. (c) Temporal intensity profile of the attosecond pulses obtained by integrating the signal between the white lines in (a) and (b). The pulse duration of individual attosecond pulses is 160 as (FWHM) without WFR (dashed line) and 240 as with WFR (solid line).

IV. DESCRIPTION OF THE MODEL

In the present study, we use a nonadiabatic model in Cartesian geometry, in a two-dimensional (2D) version—one dimension in the transverse direction and one along the longitudinal direction. We numerically solve the coupled wave equations for the fundamental and the harmonic fields, in the paraxial approximation. A detailed description of the principle of this code is given in Refs. [23–25]. In contrast to the codes described in Refs. [23–25], we do not assume cylindrical symmetry and therefore use Cartesian rather than cylindrical coordinates. This is simply achieved by changing the Laplacian operator in the equation of propagation of the laser and harmonic fields from $\nabla_\perp^2 = \frac{\partial^2}{\partial r^2} + \frac{1}{r}\frac{\partial}{\partial r}$ to $\frac{\partial^2}{\partial x^2}$. We thus briefly outline here the main stages of the calculation. We first solve the wave equation for the fundamental field which is then used for calculating the source term in the wave equation for the harmonic field. The atomic dipole moment entering the source term is calculated in the strong-field approximation (SFA), following the model described in Ref. [26]. The optical-field ionization (OFI) of the gas, leading to the depletion of the medium, to the refraction of the fundamental field, and to the electron dispersion on the harmonic field, is modeled by Ammosov-Delone-Kraïnov (ADK) tunneling rates [27]. Atomic dispersion and absorption of the gas are also taken into account in the wave equation for the harmonic field for photon energies greater than 10 eV [28]. The effect may be significant, even though we consider thin (<1 mm) targets here. The coupled wave equations are solved in the frame moving with the laser pulse, using a finite-difference scheme in space. Time derivatives are eliminated from the equations by a Fourier transform of the fields. Here, we typically use 2^8 points in time per optical cycle, which is large enough for resolving the highest frequency in the simulations. The step size is 0.5 μm in the transverse direction and 2 μm in the propagation (longitudinal) direction. The grid size is four times the target width along z. The laser beam is initialized by numerically back-propagating in vacuum the field at focus, given by Eq. (2), up to the entrance of the numerical grid. Note that we could in principle have used Eqs. (9)–(16) for calculating the initial field out of focus, but we found it much more convenient to propagate it numerically.

The results of a simulation of the attosecond lighthouse effect with this code are presented in Fig. 3(b), which displays the far-field space-time distributions of the attosecond pulses, calculated when the laser field given in Fig. 2 is used for the generation. It is compared to the results obtained in the same conditions without any WFR for ($\xi = 0$), shown in Fig. 3(a). In both cases, the peak intensity in the central part of the gas medium is 8.65×10^{14} W/cm^2. This value corresponds to the saturation intensity, $I_{\rm sat}$, of neon, the gas used in all the simulations reported hereafter. Working around the saturation intensity of the gas of generation allows one to optimize the HHG efficiency. The best focus is 200 μm ($0.5 \times z_R$) in front of a 100-μm-long super-Gaussian jet, and the maximum gas pressure in the jet is 10 mbar. The parameters used here define the reference case for the attosecond lighthouse, with which we will compare the results of the parametric study presented in Sec. V. They closely match the ones of the experiment reported in Ref. [18]. One can clearly see in Fig. 3(b) the lighthouse effect, with the generation of individual attosecond pulses propagating in different directions. Such an effect leads to modulations in the time-integrated far-field angular intensity profile, as we are going to see in detail in Sec. V. Note the very significant reduction in divergence of the attosecond pulses when WFR is applied, which is favorable for the attosecond lighthouse effect [smaller θ_q in Eq. (7)]. This reduction is partly due to the increase in the laser focal spot size associated to the application of WFR.

Figure 3(c) depicts attosecond pulses obtained by spatially integrating the signal between the white lines in Figs. 3(a) and 3(b). The duration of the central attosecond pulse generated with WFR (solid line) is 240 as (FWHM), against 160 as for the one generated without WFR (dashed line). The generation efficiency with a regular spatial and temporal Gaussian beam is a bit stronger than the one achieved with a pulse experiencing WFR, but we observed that the ratio generally hardly exceeds a factor of 2.

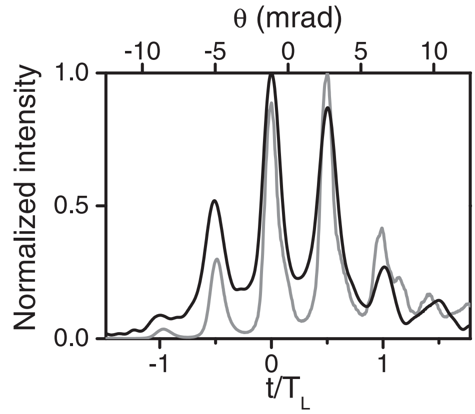

FIG. 4. Comparison of the HH time-integrated far-field angular intensity profile (black line), and the spatially integrated attosecond pulse train temporal intensity profile (gray line). Negative θ (upper scale) values correspond to early times in the pulse. The correspondence between θ and t is given by $\theta = v_r^{\max} t$, with $v_r^{\max} = 3 \times 10^{-3}$ rad/fs.

V. RESULTS AND DISCUSSION

A. Influence of HHG parameters on the lighthouse effect

As is well established now, HHG in gases is ruled by a phase-matching relation between the laser and harmonic field wave vectors, which is conveniently written as the sum of four terms, accounting for the laser focusing, the single atom response, the electron dispersion, and the atomic dispersion and absorption. The first two terms in the sum, respectively called geometric and dipole terms later on in the text, are proportional to $\nabla\phi(x,z)$ and $\nabla I_f(x,z)$ [29], respectively, where $\phi(x,z)$ is the spatially dependent phase of the laser, given by Eq. (20) with $\xi = 0$, and $I_f(x,z)$, its intensity. When $\xi \neq 0$, $\phi(x,z)$ is replaced by $\Phi(x,t,z)$ [Eq. (17)], and $I_f(x,z)$ is modified due to the stretching of the waist [Eq. (10)]. One thus expects significant changes of the geometric and dipole contributions to the phase mismatch due to STC. The two last terms in the sum can also be modified through a reduction of the ionization yields due to the decrease of the peak laser intensity induced by the stretching of the waist and of the pulse duration [Eqs. (10) and (13)].

In the study presented below, we vary the different target and laser parameters one by one, except the CEP whose effect was studied in Ref. [18], and compare the high-harmonic far-field angular intensity profile obtained in these different conditions to the one of our reference case. Considering the far-field angular intensity profile is highly relevant because this provides a direct measurement of the spatial encoding of the attosecond pulse train, as demonstrated both numerically and experimentally in Ref. [18]. These far-field intensity profiles are obtained by a time integration of the harmonic field obtained after propagation over the distance separating the exit of the generating medium from the observation plane. The propagation is achieved through a spatial Fourier transform applied to the—spectrally filtered—radiated harmonic field. The selected spectral bandwidth matches the plateau region of the harmonic spectrum, which extends here from 30- to 140-eV photon energy. The normalization of the profiles is performed relative to our reference case. Negative θ values correspond to early times in the laser pulse. Such a representation is illustrated in Fig. 4 for our reference case, that compares the temporal profile of the generated attosecond pulse train, obtained by spatially integrating the harmonic signal in the far-field (gray curve) and the time-integrated far-field angular profile (black curve). A very good qualitative matching is observed between these two curves, thus demonstrating the time-to-space mapping induced by WFR.

In the spectral range of interest here, namely the plateau region of the spectrum, the contributing trajectories are of quite generic types for high harmonics, whatever the atom. There are mainly two electron quantum paths contributing to HHG, called short and long path (or trajectory), respectively. The relative contribution of these two trajectories depends on the focus position with respect to the gas target, through the geometric and the dipole terms. When focusing in front of the gas target, the short quantum path is favored, while the long path, whose phase varies typically 25 times faster than that of the short one with laser intensity, prevails when focusing behind the target. Note that such a general trend could be modified when using a beam with PFT, since new phase terms are involved for the laser field. This point will require further studies in the future.

We have reported in Fig. 5 the evolution of HH far-field intensity profiles with focus position z_f for values of z_f/z_R ratio equal to -1.25 (a), -0.5 (reference case) (b), 0.0 (c), and $+0.5$ (d). Negative z_f values correspond to focus positions in front of the gas target. The structures in far-field profiles, characteristic of the attosecond lighthouse effect, survive for values of $|z_f/z_R| > 1$ [Fig. 5(a)], but with a slight decrease of the intensity of the peaks, which move and broaden, compared to the reference case. This is most likely due to the reduction of the WFR velocity of the driving field far from the focus. For a focus position in the middle of the medium, the peaks are well separated [Fig. 5(c)], like in the reference case [Fig. 5(b)]. By contrast, when focusing behind the target [Fig. 5(d)], at a symmetric position to our reference case [Fig. 5(b)], the peaks broaden again. However, in that case, the modifications in the profile are due to the geometric and dipole contributions to the phase mismatch. As previously stated, when focusing behind the target, the long trajectory, whose divergence is much larger than the short one, dominates the emission, and hence, the condition given by Eq. (7) is no longer fulfilled.

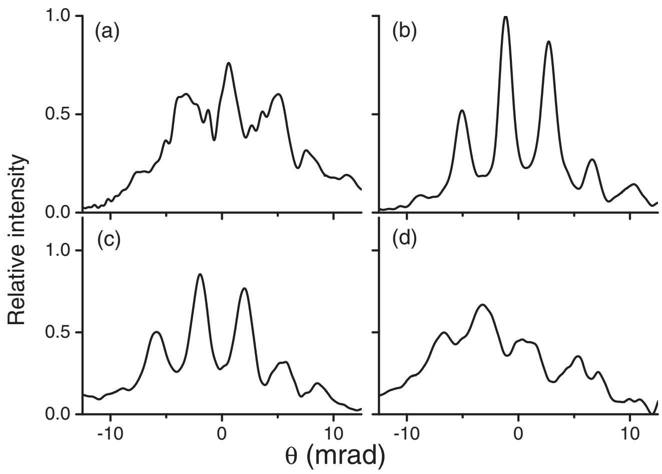

FIG. 5. Evolution of HH (relative) far-field intensity profile with focus position for (a) $z_f/z_R = -1.25$, (b) -0.5, (c) 0.0, and (d) $+0.5$. Negative values of z_f/z_R correspond to focus positions in front of the gas target. Normalization is performed with respect to our reference case, displayed in (b). See text for details.

For optimizing the harmonic signal, it may be beneficial to increase the length of the medium. We observe that the far-field profile then rapidly gets degraded when increasing the target width beyond the Rayleigh range, as shown in Fig. 6, which depicts HH far-field profiles calculated for values of L_{med}/z_R

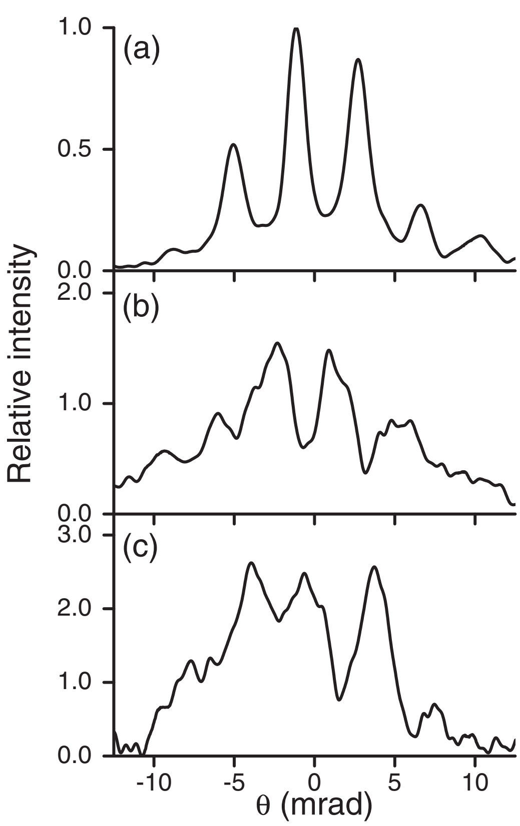

FIG. 6. Influence of the medium length on HH far-field intensity profile for $I_L(x = z = 0) = I_{\mathrm{sat}}$, $\tau_L = 5$ fs, $P = 10$ mbar, and (a) $L_{\mathrm{med}}/z_R = 0.25$ (reference case), (b) 1.25, and (c) 2.5.

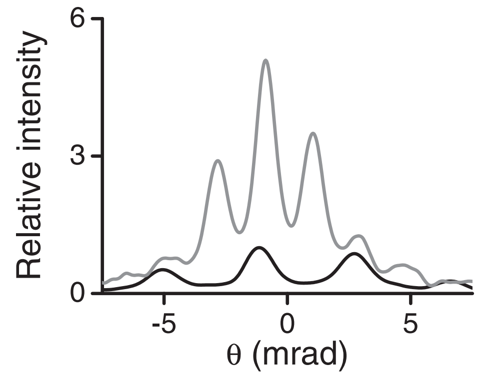

FIG. 7. Evolution with focal length of HH far-field intensity profile. $I_L(x = z = 0) = I_{\mathrm{sat}}$, $\tau_L = 5$ fs, and $P = 10$ mbar. Black curve: $f = 1$ m (reference case). Gray curve: $f = 2$ m.

ratio ranging from 0.25 to 2.5. The peaks merge while their intensity globally increases with target length.

One can overcome this problem by increasing the Rayleigh range of the focused beam. The most straightforward way for doing so is to increase the focal length of the focusing optics. This of course slows down the WFR velocity, whose maximum value scales as f^{-1}. But this simultaneously decreases the laser beam divergence θ_L, and hence the harmonic divergence θ_q (assuming a constant ration θ_q/θ_L when the focal length is changed). This is why the separation criterion given by Eq. (7) does not depend on the focal length parameter—this parameter is thus not expected to affect the quality of the angular separation of the beamlets produced by attosecond lighthouse effect. To confirm this prediction, Fig. 7 shows HH far-field intensity profiles calculated for $f = 1$ m and $f = 2$ m optics. Due to the smaller rotation velocity, the overall divergence of the collection of beamlets is divided by a factor of 2 when doubling the focal length. But the divergence of individual beamlets is also reduced by a factor of about 2, so that the individual peaks are still well separated. As expected, we observed that with a 2-m focal length optics, the attosecond lighthouse effect is less sensitive to a change of focus position or/and to an increase of medium length, as compared to the case when a 1-m focal length optics is used. The robustness of attosecond lighthouses against variations of focus position and/or target length can thus be significantly improved by increasing the Rayleigh range of the beam, hence favoring WFR on PFT. As in usual HHG experiments, the limit on the beam Rayleigh length is only imposed by the energy of the driving laser pulse, which has to be high enough to reach the intensities required for efficient HHG.

When varying the laser intensity, one affects the degree of ionization of the medium. This impacts the phase matching at different levels. By changing the electron density, one modifies the electron and atomic dispersions of the medium, as well as the number of emitters inside the interaction volume. This could also disturb, both spatially and spectrally, the driving laser field, resulting in modifications of the geometric and dipole terms in the phase-matching relation. For intensities well below the saturation intensity of the gas [Fig. 8(a)], the electron dispersion is negligible, and the attosecond pulse emissions occur near the maximum of the laser pulse. When

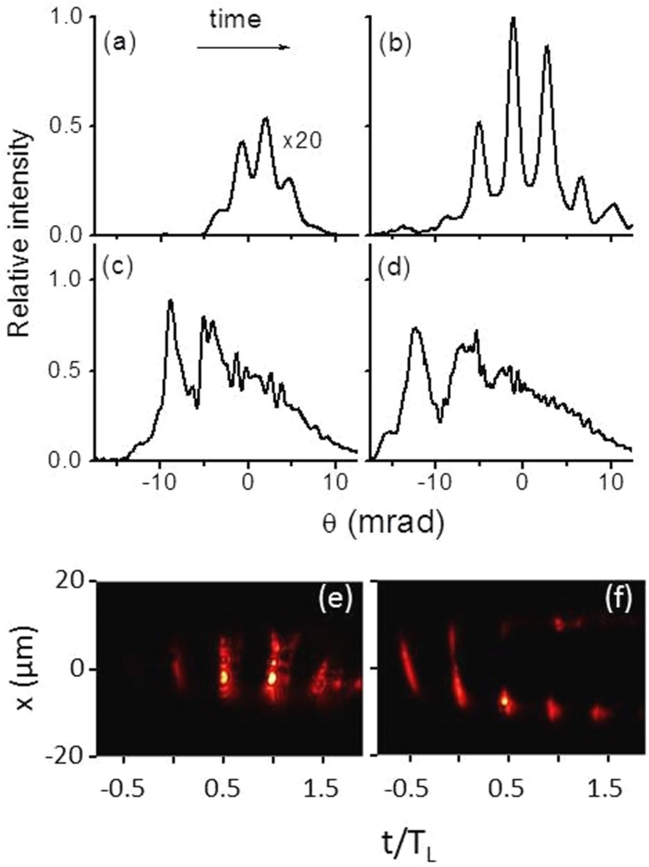

FIG. 8. HH far-field intensity profile calculated for $P = 10$ mbar, $\tau_L = 5$ fs, and (a) $I_L(x = z = 0) = 0.6 \times I_{\text{sat}}$, (b) I_{sat} (reference case), (c) $2 \times I_{\text{sat}}$, and (d) $4 \times I_{\text{sat}}$. The arrow indicates the time direction. Panels (e) and (f) display the spatiotemporal intensity distributions of the attosecond pulses in the middle of the gas medium (in $z = 0$) for $I_L(x = z = 0) = I_{\text{sat}}$ [case of panel (b)] and $2 \times I_{\text{sat}}$ [case of panel (c)], respectively.

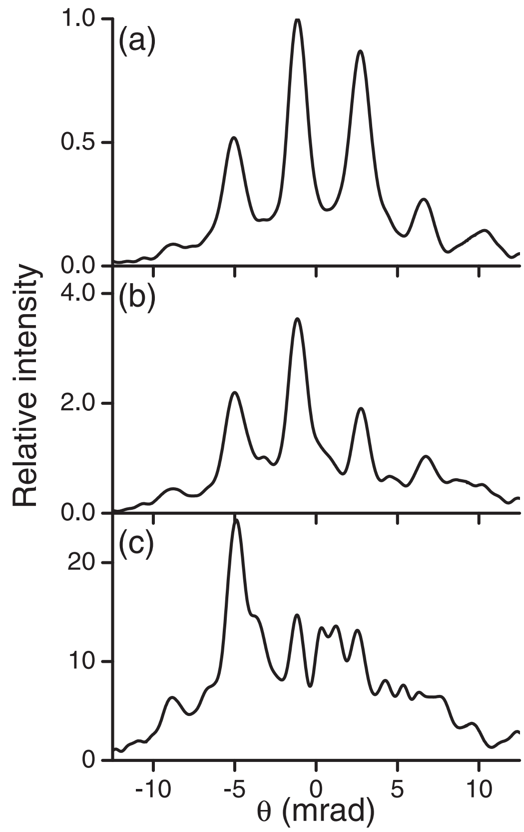

FIG. 9. Evolution with pressure of HH far-field intensity profile. $I_L(x = z = 0) = I_{\text{sat}}$ and $\tau_L = 5$ fs. (a) $P = 10$ mbar (reference case). (b) $P = 20$ mbar. (c) $P = 80$ mbar.

increasing the laser intensity to I_{sat}, and beyond, the emission moves towards the leading front of the pulse. For laser intensities exceeding the saturation intensity of the gas, a single bright peak emerges whose position shifts towards large negative angles (corresponding to early times in the laser pulse) with increasing intensity [see Figs. 8(c) and 8(d)]. This indicates that harmonics are efficiently emitted earlier and earlier in the pulse with increasing intensity, before the gas target is fully ionized.

This peak is followed by a slightly weaker quasicontinuous signal, which one might attribute to a loss of the attosecond temporal structure of the emission. This is however not the case, as illustrated in Figs. 8(e) and 8(f). These two panels compare the spatiotemporal intensity distribution of the harmonic field in the middle of the gas medium (in $z = 0$) for $I_L(x = z = 0) = I_{\text{sat}}$ and $2 \times I_{\text{sat}}$. Due to the spatiotemporal dependence of the ionization, for $I_L = 2 \times I_{\text{sat}}$ (f), harmonics are first emitted on the leading front of the pulse, resulting in the initial bright peak in Fig. 8(c) and, later in the laser pulse, are only generated in the spatial wings of the beam. This more localized spatial distribution of the source implies a much larger divergence for these subsequent attosecond pulses. As a result, the separation criterion Eq. (7) is no longer satisfied for these pulses, and the simple time-to-angle mapping of the attosecond lighthouse effect is lost in this time range. In this regime, the angular profile of the harmonic beam no longer provides reliable information on the temporal structure of the emission after the rising edge of the pulse. Note that we verified that in this parameter range, the spatial and temporal shapes of the laser (not shown here) remain unchanged whatever the intensity used: it is only the harmonic field that is affected by the ionization of the medium, not the driving field.

Increasing the gas pressure from 10 to 80 mbar also leads to strong distortions of the HH far-field intensity profile, as shown in Fig. 9. However, in this case, the decrease of the signal after the initial bright peak at the leading front of the pulse rather comes from the wave vector mismatch due to the free electrons, whose density, and hence dispersion, scale linearly with pressure. Here, the electron dispersion is not compensated by the atomic dispersion; the latter remains low in the conditions of generation we consider (short medium), even for the highest gas pressure.

One can control and optimize the lighthouse effect through variations of the STC parameter. As discussed in Sec. II, this changes the maximum WFR velocity of the driving laser field as well as its variation along the propagation axis, thus modifying the phase-matching relation. We now test the influence of small variations of v_r around $v_r^{\max}$ on attosecond lighthouses. The results are reported in Fig. 10. Figure 10(a)

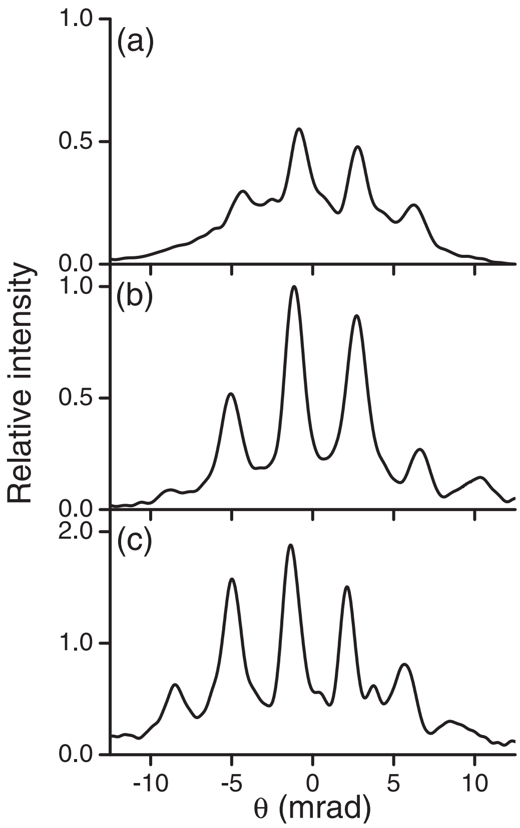

FIG. 10. Dependence of HH far-field intensity profile on STC parameter. $I_L(x = z = 0) = I_{\text{sat}}$ and $P = 10$ mbar. (a) $\xi = \frac{2}{3} \times \xi_{\max}$. (b) $\xi = \xi_{\max}$ (reference case). (c) $\xi = \frac{3}{2} \times \xi_{\max}$.

corresponds to the case $\xi = \frac{2}{3} \times \xi_{\max}$, whereas the curve in Fig. 10(c) was obtained for $\xi = \frac{3}{2} \times \xi_{\max}$. Both are compared to the reference case $\xi = \xi_{\max}$ [Fig. 10(b)]. A significant change is observed in the far-field profiles between the two cases $\xi = \frac{2}{3} \times \xi_{\max}$ and $\frac{3}{2} \times \xi_{\max}$, although the WFR velocity at focus is 90% of $v_r^{\max}$ (see Fig. 1) in both cases. A significantly stronger signal is in particular observed for $\xi = \frac{3}{2} \times \xi_{\max}$. This can be attributed to the increase of the effective Rayleigh range with ξ [Eq. (12)]. This shows that attosecond lighthouses in gases should preferentially be driven with $\xi \gtrsim \xi_{\max}$, provided the associated reduction in peak intensity can be compensated with a higher input energy of the laser pulse.

So far, we considered extremely short laser pulses, that are typically obtained using postcompression techniques. However, it would be interesting to generalize the previous results to longer pulses, so as to make attosecond lighthouses accessible to a broader community. The main problem is that increasing the laser pulse duration reduces the WFR velocity. An increase by a factor of 2 of the pulse duration divides the maximum WFR velocity by a factor of 2, thus doubling the number of attosecond pulses in a given angle range, as shown on the gray curve in Fig. 11. The angular separation of the peaks is thus degraded. The decrease in HH intensity observed for $\tau_L = 10$ fs is due to the increase of the gas ionization with pulse duration at the leading edge of the pulse.

Finally, we studied the influence of the spatial intensity profile of the laser beam prior to focusing. Indeed, in all analytical calculations, this profile is assumed to be Gaussian,

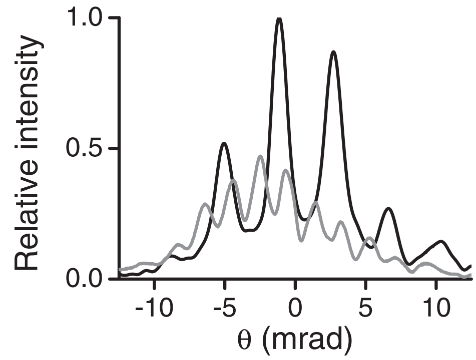

FIG. 11. HH far-field intensity profiles calculated for $\tau_L = 5$ fs, $\xi = 0.17$ fs/mm (black line, reference case), and $\tau_L = 10$ fs, $\xi = 0.34$ fs/mm (gray line). $I_L(x = z = 0) = I_{\text{sat}}$ and $P = 10$ mbar.

while it is typically closer to a top-hat beam in experiments. We thus chose a flat-top spatial profile, and compared the results to our Gaussian reference case. The comparison, displayed in Fig. 12, shows little difference between flat-top and Gaussian initial spatial beam profiles.

B. Lighthouse effect with midinfrared and two-color pulses

In order to relax the requirement on pulse duration for producing attosecond lighthouses in gases, we studied different schemes using midinfrared (MIR) and/or a combination of two-color laser pulses, in the same spirit as the two-color gating [30,31], and further derived schemes, like double-optical gating (DOG) [13] and generalized-double-optical gating (GDOG) [14]. The key idea in a two-color experiment is to increase the time separation between successive attosecond pulses in the train produced with multicycles lasers, in order to facilitate the isolation of a single pulse. To this end, one generally uses a combination of ω_L and $2\omega_L$ frequency fields. The high-frequency field is used as a dressing field to the low-frequency driving field for controlling electron trajectories on a subcycle time scale. Depending on the relative phase between the two fields, one can thus select electron trajectories in order to obtain a single emission per cycle. On the other hand, the idea of using MIR pulses is actually very simple: for a given pulse duration, the number of optical cycles

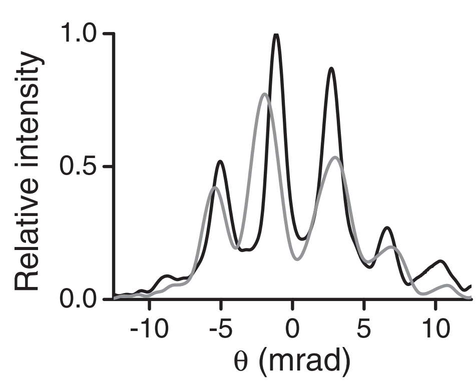

FIG. 12. Influence of spatial laser beam shape on HH far-field intensity profile. $I_L(x = z = 0) = I_{\text{sat}}$ and $P = 10$ mbar. Black line: Gaussian (reference case). Gray line: flat-top.

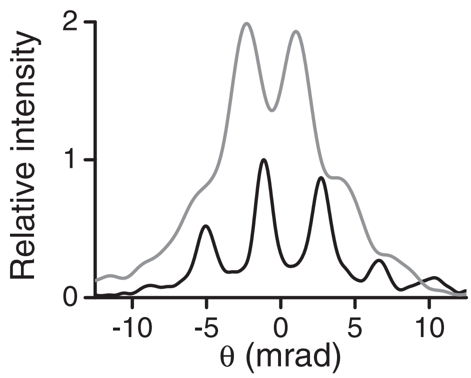

FIG. 13. Comparison between the HH intensity far-field profile obtained by mixing 400 and 800-nm wavelength fields of 10-fs duration ($\xi = 0.34\,\text{fs/mm}$) (gray line) and our reference case (black line). $I_L(\lambda_L = 800\text{ nm}) = I_{\text{sat}}$ and $I_L(\lambda_L = 400\text{ nm}) = 0.1 \times I_{\text{sat}}$ in $x = z = 0$.

decreases with increasing wavelength. Thus, one expects to obtain approximately the same result with, e.g., a 5-fs pulse duration, 800-nm wavelength laser on the one hand, and a 10-fs duration, 1600-nm wavelength laser, on the other hand. Using drivers in the MIR wavelength range is also attractive for generating very broadband harmonic spectra, extending up to the water window, and consequently very short attosecond pulses. It was however predicted that the harmonic yield would scale as $\lambda_L^{-(5\text{–}6)}$ [32], at constant driving laser intensity, and the dipole phase as λ_L^3 [33], making HHG with long-wavelength drivers very challenging. In the gas jet generation configuration relevant for the attosecond lighthouse scheme, this trend has been confirmed experimentally [34].

We first report results on a configuration using 400 and 800-nm wavelength copropagating pulses of 10-fs initial duration. The dressing ultraviolet (UV) pulse is purely Gaussian ($\xi = 0$) whereas the near-infrared (NIR) one has WFR, with optimum $\xi = 0.34\,\text{fs/mm}$. Note that such a configuration has already been successfully explored in lighthouse experiments in gases [35], but with 5-fs initial duration NIR pulses. The intensity of the UV beam is 10% that of the NIR ($I_L = I_{\text{sat}}$ in the middle of the gas jet). The relative phase between the two pulses has been set to zero. Other conditions are the same as for our reference case. The resulting far-field intensity profile is reported in Fig. 13 (gray line) and is compared to our 5-fs duration reference case (black line). The modulation has the same periodicity with the 10-fs duration bichromatic field as with the 5-fs duration NIR field alone. The factor of 2 on the pulse duration is compensated by the blocking of one of the two electron quantum paths per cycle of the NIR. The use of an additional $2\omega_L$ frequency field thus allows us to relax the constraint on the pulse duration of the NIR driving field by a factor of 2, despite the fact that only the NIR pulse has WFR. The worsening of contrast and the global increase of HH intensity could be explained by the absence of WFR on the UV dressing pulse: the UV pulse alone produces a strong background in the 30–90-eV photon energy range. This background could certainly be reduced by decreasing the intensity in the UV pulse and/or by varying the relative phase between the NIR and UV pulses. Finally, note that the background could be overestimated because the dipole is calculated in the strong-field approximation, which is marginally valid for 400-nm driving wavelength.

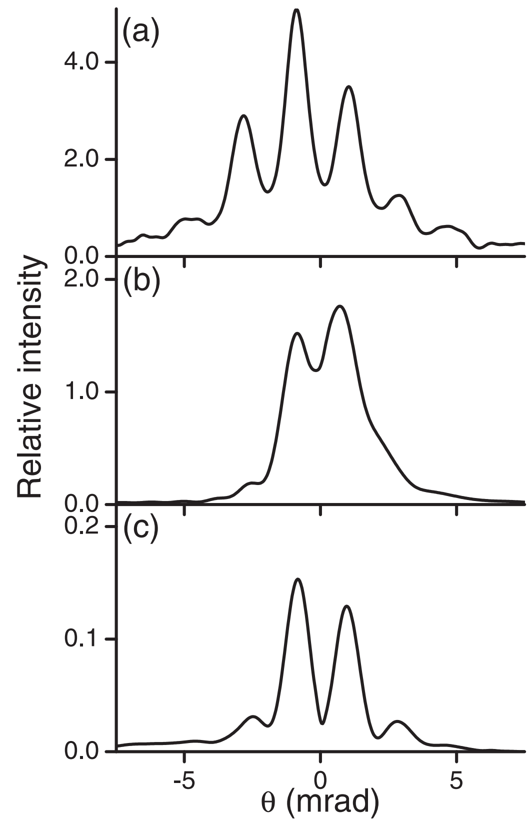

FIG. 14. HH intensity far-field profiles calculated for a $\tau_L =$ 5-fs, $\lambda_L = 800$-nm laser field (a) ($f = 2\text{m}$), (b) a $\tau_L = 10$-fs, $\lambda_L = 1600$-nm field ($\xi = 0.34\,\text{fs/mm}$), and (c) a 20-fs duration bichromatic field obtained by mixing 800 and 1600-nm wavelength ($\xi = 0.68\,\text{fs/mm}$). In the first two cases, $I_L = I_{\text{sat}}$ in $x = z = 0$, while in the latter one, $I_L(\lambda_L = 800\text{ nm}) = 0.1 \times I_{\text{sat}}$.

We next consider the production of attosecond lighthouses with a 10-fs duration, 1600-nm wavelength laser pulse of $I_L(x = z = 0) = I_{\text{sat}}$, alone. Such a short pulse is at the frontier of currently available systems operating in the MIR range [36]. Despite the above-mentioned difficulty for fulfilling the phase-matching condition with long-wavelength drivers, in the conditions of generation considered here, the intensity of the brightest peak in the HH far-field profile obtained with the MIR laser field alone [Fig. 14(b)] is only a factor of 3 smaller than the one calculated with a NIR field of same divergence [Fig. 14(a)]. The important point is that the contrast of the peaks gets worse with laser wavelength. Only two peaks can be observed on the profile corresponding to the MIR pulse, with a peak-to-valley ratio of 1.5, against almost four with the NIR field. This overlapping of adjacent beamlets is likely due to the condition on the divergence angles, given by Eq. (7), which is marginally fulfilled here. This is due to the fact that for given harmonic photon energy and beam aperture, the dipole phase—giving the wave-front curvature in the far field—scales as λ_L^3 while the laser divergence scales as λ_L^{-1}. The ratio of harmonic and laser divergence thus tends to increase with the driver wavelength, making it more and more difficult to separate the beamlets for larger wavelengths. Note that one could force condition Eq. (7) by reducing the bandwidth to low-order harmonics, since harmonic divergence increases with order, but this would lead, in turn, to an increase of attosecond pulse durations.

We finally use a combination of 800 and 1600-nm wavelength beams, for improving the contrast of the modulations and for increasing the pulse duration. As in the scheme using a mixing of UV and NIR pulses, only the driving MIR beam has WFR, with $\xi = \xi_{\max} = 0.68$ fs/mm. The dressing NIR pulse intensity is 10% of the MIR one, the latter being equal to $I_{\rm sat}$ in the middle of the gas target. We assume a zero relative phase between the dressing and the driving fields. Both of them have 20-fs pulse duration. The resulting HH far-field intensity profile is given in Fig. 14(c). We first observe that attosecond lighthouse effect still exists with 20-fs duration pulses, showing that it can be obtained with currently available lasers without pulse postcompression. Second, we note a significant improvement of the contrast, compared to that obtained with the 10-fs duration MIR field alone. We also observe a drastic drop of efficiency, indicating that phase matching is difficult to achieve in this case. Further investigations are thus required for optimizing the emission while preserving the lighthouse effect. One could, for instance, play on the ratio between NIR and MIR pulse intensities or/and on the relative phase between the two pulses.

VI. SUMMARY

In summary, we have presented an extensive study on the attosecond lighthouse effect in gases. We derived analytical expressions describing the laser field with STC out of focus, assuming linear propagation. These can be used to qualitatively understand how the different laser and interaction parameters (e.g., the PFT coefficient or the medium length) affect the attosecond lighthouse effect in gases. We then performed a parametric numerical study, which aimed at testing the robustness of this effect against variations of high-harmonic generation parameters on the one hand, and at relaxing the requirement on the driving laser pulse duration on the other. The optimal results (Figs. 3 and 4) were obtained for a thin, 100-μm-long, gas target ($L_{\rm med}/z_R = 0.25$), thereby favoring wave-front rotation on pulse front tilt, and a laser focus position 200 μm in front of the target ($z_f/z_R = -0.5$), thus promoting the phase matching of the short electron quantum path in the emission process. As in standard cases, higher signals can be obtained using longer focal lengths (Fig. 7), provided the laser intensity can be maintained. The attosecond lighthouse effect is not sensitive to pressure variations in the 10–20-mbar range nor to the incident laser beam spatial profile. By contrast, it is quite sensitive to deviations from the optimum space-time coupling parameter, and our study revealed that using a pulse front tilt parameter slightly larger than the one that maximizes the wave-front rotation velocity can be beneficial, due to the increase in effective Rayleigh length. Of course, the shorter the laser pulse duration, the better the separation of adjacent beamlets. However, partial separation is still observed when increasing the pulse duration from 5 to 10 fs. In the last part of the paper, we demonstrated that it was even possible to increase the pulse duration of the driving laser to 20 fs, by mixing midinfrared and near-infrared fields, thus making the use of the attosecond lighthouse effect accessible to a broad community.

[1] G. Sansone, L. Poletto, and M. Nisoli, Nat. Photon. **5**, 655 (2011).
[2] Y. Mairesse and F. Quéré, Phys. Rev. A **71**, 011401 (2005).
[3] P. M. Paul, E. S. Toma, P. Breger, G. Mullot, F. Augé, Ph. Balcou, H. G. Muller, and P. Agostini, Science **292**, 1689 (2001).
[4] M. Hentschel, R. Kienberger, Ch. Spielmann, G. A. Reider, N. Milosevic, T. Brabec, P. Corkum, U. Heinzmann, M. Drescher, and F. Krausz, Nature (London) **414**, 509 (2001).
[5] F. Lépine, M. Y. Ivanov, and M. J. J. Vrakking, Nat. Photon. **8**, 195 (2014).
[6] A. L. Cavalieri, N. Muller, Th. Uphues, V. S. Yakovlev, A. Baltuska, B. Horvath, B. Schmidt, L. Blumel, R. Holzwarth, S. Hendel, M. Drescher, U. Kleineberg, P. M. Echenique, R. Kienberger, F. Krausz, and U. Heinzmann, Nature (London) **449**, 1029 (2007).
[7] P. B. Corkum, N. H. Burnett, and M. Y. Ivanov, Opt. Lett. **19**, 1870 (1994).
[8] G. Sansone, E. Benedetti, F. Calegari, C. Vozzi, L. Avaldi, R. Flammini, L. Poletto, P. Villoresi, C. Altucci, R. Velotta, S. Stagira, S. De Silvestri, and M. Nisoli, Science **314**, 443 (2006).
[9] E. Goulielmakis, M. Schultze, M. Hofstetter, V. S. Yakovlev, J. Gagnon, M. Uiberacker, A. L. Aquila, E. M. Gullikson, D. T. Attwood, R. Kienberger, F. Krausz, and U. Kleineberg, Science **320**, 1614 (2010).
[10] H. Merdji, T. Auguste, W. Boutu, J.-P. Caumes, B. Carré, T. Pfeifer, A. Julien, D. M. Neumark, and S. R. Leone, Opt. Lett. **32**, 3134 (2007).
[11] P. Lan, E. J. Takahashi, and K. Midorikawa, Phys. Rev. A **82**, 053413 (2010).
[12] E. J. Takahashi, P. Lan, O. D. Mücke, Y. Nabekawa, and K. Midorikawa, Phys. Rev. Lett. **104**, 233901 (2010).
[13] H. Mashiko, S. Gilbertson, C. Li, S. D. Khan, M. M. Shakya, E. Moon, and Z. Chang, Phys. Rev. Lett. **100**, 103906 (2008).
[14] X. Feng, S. Gilbertson, H. Mashiko, H. Wang, S. D. Khan, M. Chini, Y. Wu, K. Zhao, and Z. Chang, Phys. Rev. Lett. **103**, 183901 (2009).
[15] S. Akturk, X. Gu, P. Bowlan, and R. Trebino, J. Opt. **12**, 093001 (2010).
[16] H. Vincenti and F. Quéré, Phys. Rev. Lett. **108**, 113904 (2012).
[17] J. A. Wheeler, A. Borot, S. Monchocé, H. Vincenti, A. Ricci, A. Malvache, R. Lopez-Martens, and F. Quéré, Nat. Photon. **6**, 829 (2012).
[18] K. T. Kim, C. Zhang, T. Ruchon, J.-F. Hergott, T. Auguste, D. M. Villeneuve, P. B. Corkum, and F. Quéré, Nat. Photon. **7**, 651 (2013).
[19] F. Quéré, H. Vincenti, A. Borot, S. Monchocé, T. J. Hammond, K. T. Kim, J. A. Wheeler, C. Zhang, T. Ruchon, T. Auguste, J.-F.

Hergott, D. M. Villeneuve, P. B. Corkum, and R. Lopez-Martens, J. Phys. B **47**, 124004 (2014).
[20] C. Zhang, G. Vampa, D. M. Villeneuve, and P. B. Corkum, J. Phys. B **48**, 061001 (2015).
[21] F. Silva, S. M. Teichmann, S. L. Cousin, M. Hemmer, and J. Biegert, Nat. Commun. **6**, 6611 (2015).
[22] K. Iizuka, *Engineering Optics*, 3rd ed., Springer Series in Optical Sciences Vol. 35 (Springer, New York, 2008).
[23] E. Priori, G. Cerullo, M. Nisoli, S. Stagira, S. De Silvestri, P. Villoresi, L. Poletto, P. Ceccherini, C. Altucci, R. Bruzzese, and C. de Lisio, Phys. Rev. A **61**, 063801 (2000).
[24] M. B. Gaarde, K. J. Schafer, A. Heinrich, J. Biegert, and U. Keller, Phys. Rev. A **72**, 013411 (2005).
[25] M. B. Gaarde, J. L. Tate, and K. J. Schafer, J. Phys. B **41**, 132001 (2008).
[26] M. Lewenstein, Ph. Balcou, M. Yu. Ivanov, A. L'Huillier, and P. B. Corkum, Phys. Rev. A **49**, 2117 (1994).
[27] M. V. Ammosov, N. B. Delone, and V. P. Kraïnov, Zh. Eksp. Teor. Fiz. **91**, 2008 (1986) [Sov. Phys. JETP **64**, 1191 (1986)].
[28] B. L. Henke, E. M. Gullikson, and J. C. Davis, At. Data Nucl. Data Tables **54**, 181 (1993).
[29] Ph. Balcou, P. Salières, A. L'Huillier, and M. Lewenstein, Phys. Rev. A **55**, 3204 (1997).
[30] T. Pfeifer, L. Gallmann, M. J. Abel, P. M. Nagel, D. M. Neumark, and S. R. Leone, Phys. Rev. Lett. **97**, 163901 (2006).
[31] P. Lan, P. Lu, W. Cao, Y. Li, and X. Wang, Phys. Rev. A **76**, 011402(R) (2007).
[32] J. Tate, T. Auguste, H. G. Muller, P. Salières, P. Agostini, and L. F. DiMauro, Phys. Rev. Lett. **98**, 013901 (2007).
[33] K. Schiessl, K. L. Ishikawa, E. Persson, and J. Burgdörfer, Phys. Rev. Lett. **99**, 253903 (2007).
[34] A. D. Shiner, C. Trallero-Herrero, N. Kajumba, H.-C. Bandulet, D. Comtois, F. Légaré, M. Giguère, J.-C. Kieffer, P. B. Corkum, and D. M. Villeneuve, Phys. Rev. Lett. **103**, 073902 (2009).
[35] T. J. Hammond, K. T. Kim, C. Zhang, D. M. Villeneuve, and P. B. Corkum, Opt. Lett. **40**, 1768 (2015).
[36] B. E. Schmidt, A. D. Shiner, P. Lassonde, J.-C. Kieffer, P. B. Corkum, D. M. Villeneuve, and F. Légaré, Opt. Express **19**, 6858 (2011).